Effects of operating parameters on in-cylinder flow characteristics of an optically accessible engine with a spray-guided injector

Donghwan Kim [a], Yousang Son [b], Sungwook Park [c], *

[a] *Department of Mechanical Convergence Engineering, Graduate School of Hanyang University, Seoul, 04763, Republic of Korea*
[b] *Engine Advanced Development Team, Hyundai Motor Group, Gyeonggi-do, 18280, Republic of Korea*
[c] *School of Mechanical Engineering, Hanyang University, Seoul, 04763, Republic of Korea*

ARTICLE INFO

ABSTRACT

This study investigated the cycle-to-cycle variation of a spark-assist high-compression-ratio spray-guided direct-injection two-cylinder optically accessible engine. The cycle-to-cycle variation was evaluated by calculating the mean velocity, tumble ratio, tumble center, and effective radius using the PIV measurement results. Under all experimental conditions, the mean velocity continuously decreased owing to the momentum loss from the intake to compression strokes. A low COV was observed within the high-velocity region, and the effective radius decreased as rotational flow formed regardless of the engine operating conditions. As the engine speed increased, owing to the high piston speed, the in-cylinder flow intensified. However, the effective radius and tumble ratio were similar during the compression stroke. As the intake pressure increased from 0.8 to 1.3 bar, the mean velocity and tumble ratio slightly increased. Moreover, the effective radius decreased slightly during the compression stroke. As the IVO timing was retarded, during the intake stroke, the structure of the in-cylinder flow changed dramatically. Rapid momentum dissipation occurred after the intake air inflowed strongly, resulting in relatively weak rotational flow compared to the reference and advanced IVO timing conditions.

1. Introduction

To increase engine performance while meeting the strict emission regulations of an internal combustion engine [1], many previous studies have been conducted on new combustion strategies [2]. In a spray-guided stratified charge engine, a relatively late injection with center injection is applied to form a stratified mixture [3,4]. This stratified mixture allows the engine to operate under lean conditions. The associated advantages include lower pumping loss, lower gas temperature, and higher thermal efficiency [5]. However, owing to the late injection, there is an increasing probability of wall wetting and fuel impingement [6]. Research on spray-guided stratified charge engines has been conducted to utilize the advantages and overcome the limitations. For example, Geschwindner et al. combined DBI and Mie scattering imaging techniques and PIV measurements to analyze the interaction between spray and in-cylinder flow in a spray-guided direct injection

optically accessible engine [7]. They found that the in-cylinder flow velocity magnitude was increased by fuel injection, and the in-cylinder flow could not affect the spray structure under test conditions. However, the influence of the in-cylinder flow on the spray development should be considered if the gas density increases. Kazmouz et al. investigated a large eddy simulation of a stratified-charge direct-injection spark-ignition engine in a highly stratified late injection mode [8]. The results showed that vapor fuel distribution is an important factor for flame development. The in-cylinder flow could be intensified by injection events, especially at the edge of the spray jet. The spray can lead to unfavorable conditions, such as misfire and slow burn.

In homogeneous charge compression ignition (HCCI) engines, which have a high compression ratio, spontaneous auto-ignition combustion is used to achieve low emissions and high combustion efficiency [9]. However, there are also fatal problems, such as knocking and noise, auto-ignition timing, and combustion phase. It

---

* Corresponding author. School of Mechanical Engineering, Hanyang University, 222 Wangsimni-ro, Seongdong-gu, Seoul, 04763, Republic of Korea.
E-mail address: parks@hanyang.ac.kr (S. Park).

is difficult to control combustion because combustion occurs without a spark plug in the HCCI engine [10]. In particular, as the auto-ignition timing and combustion phase are influenced by many factors, such as fuel properties, physical properties, air temperature, and in-cylinder pressure, it is difficult to control and understand them [2,11]. Therefore, researchers have investigated HCCI engine performance to develop a better understanding and control. Parthasarathy et al. investigated the performance of an HCCI engine powered by tamanu methyl ester, considering inlet air temperature and exhaust gas recirculation ratios, and compared the HCCI engine to a conventional compression ignition (CI) engine [12]. They found that the brake thermal efficiency of a conventional CI engine was higher than that of an HCCI engine owing to the lean-burn condition of HCCI combustion. The fuel economy of the CI engine was also higher than that of the HCCI engine, along with less carbon monoxide and unburned hydrocarbon emissions. They optimized the inlet air temperature to 90 °C in an HCCI engine. Aydogan also studied the performance and emission characteristics of an HCCI engine as a function of the fuel properties [13]. An experimental comparison of the blending ratios of n-hexane and heptane fuel was conducted. They tried to solve the problems of knocking and misfiring using the charge mixture composition. They found that the in-cylinder pressure decreased with the increase in lambda under all test conditions, and the thermal efficiency was highest in the case of the leaner charge mixture containing 75% n-heptane and 25% n-hexane owing to the higher fraction of n-heptane, which has a low octane number.

To overcome the disadvantages of the HCCI engine, a spark-controlled compression ignition (SPCCI) engine was developed by Mazda [14]. Mazda solved the main problems such as auto-ignition timing and cold start with the use of a spark and injection strategy. In an SPCCI engine, a pre-ignition that can damage the engine is controlled by a multiple-injection strategy and combustion can be stabilized using a spark plug. However, although the SPCCI engine is an advancement to the HCCI engine and is commercialized, its operating range remains limited. Therefore, a new combustion mode is yet to be optimized and requires further research. In this study, to employ the characteristics of auto-ignition for combustion, a test engine with a high compression ratio was used. Additionally, to gain advantages of operating the engine under lean-burn conditions, a piston shape with a bowl and spray-guided injection system was used to form a stratified mixture. Moreover, the combustion stability was secured by mounting a spark plug. To optimize the combustion strategy, a fundamental understanding is required; therefore, the in-cylinder flow characteristics and cycle-to-cycle variation (CCV) of a spark-assist high-compression-ratio spray-guided direct-injection optically accessible engine were analyzed under various engine operating conditions using PIV measurements. The in-cylinder flows were visualized depending on the engine speed, intake pressure, and intake valve open (IVO) timing, which are basic operating engine parameters. Quantitative indices, such as mean velocity, tumble center (TC), tumble ratio (TR), and effective radius, were derived to analyze the CCV.

2. Experimental setup

2.1. Optically accessible engine

PIV measurements were implemented in a four-valve, two-cylinder optically accessible engine. Transparent quartz was used in both cylinders, but the visualization was conducted using only one

Table 1
Specifications of the optically accessible engine.

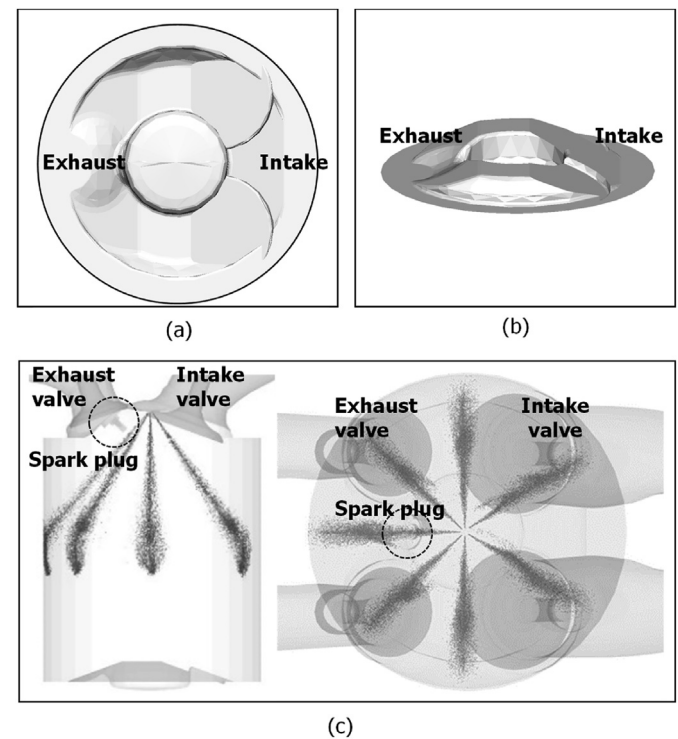| Items	Details
Bore (mm)	75.6
Radius of crank (mm)	41.6
Stroke (mm)	83.38
Displacement volume of two cylinders (cc)	748.5
Length conrod (mm)	147.8
Compression height (mm)	27.5
Height of block (mm)	217.0
Piston topping (mm)	0.33
Crank offset (mm)	10
Piston pin offset (mm)	0.7
Stroke/Bore ratio (−)	1.10
Compression ratio (−)	14

Fig. 1. Structure of the piston head and spray: (a) top-view of the piston head, (b) front view of the piston head, and (c) spray structure.

cylinder. Rulon piston rings were used instead of lubricant oil to increase the quality of the PIV raw images. The optically accessible engine has a relatively high compression ratio of 14 compared to a traditional GDI engine [15]. The specifications of the optically accessible engine are listed in Table 1.

The structures of the piston head and spray are shown in Fig. 1. The piston has a convex shape around the bowl to increase the compression ratio, as shown in Fig. 1(a) and (b). The bowl was applied to form a stratified mixture by considering the situation in which the engine was operated under lean combustion conditions. A high-pressure spray-guided injector with seven holes was mounted between the exhaust and intake valves to improve the mixing performance and apply various injection strategies, as shown in Fig. 1 (c). The spark plug was located between exhaust valves. Three plumes were developed in the direction of the
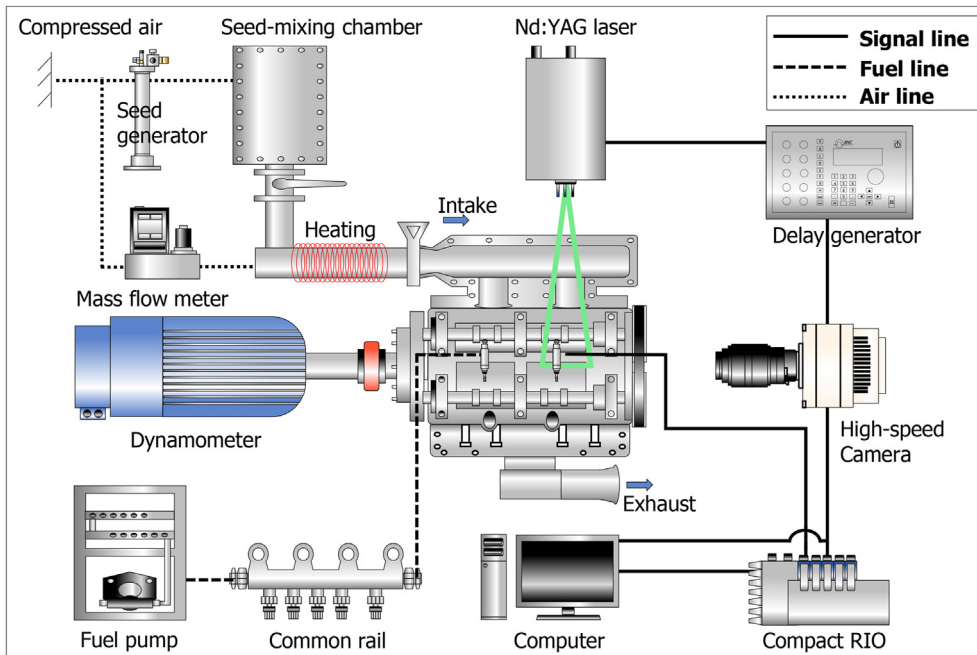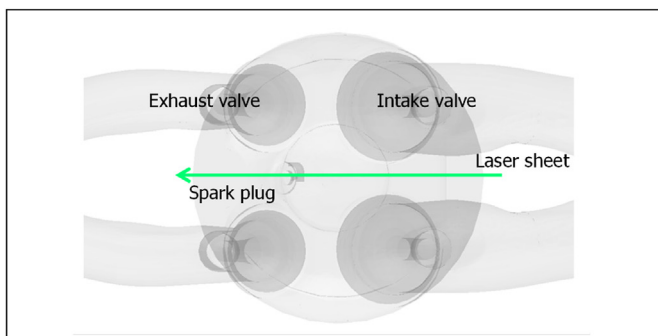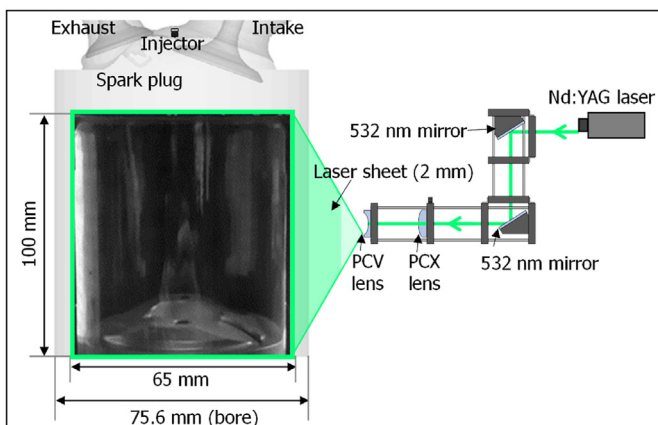
Fig. 2. Schematic of the optically accessible engine.

(a)

(b)

Fig. 3. Configuration of the PIV system: (a) location of the laser sheet and (b) configuration of the laser system.

exhaust valves, accounting for the location of the spark plug.

The schematic of the optically accessible engine is shown in Fig. 2. The intake air was supplied through a mass flow meter to control the intake pressure. Seeds (10 μm, hollow sphere glass) were generated using a seed generator. A high-speed camera (Phantom, VEO 710L) was used to visualize the in-cylinder flow. The optically accessible engine was controlled using an NI compact RIO. To capture the PIV images at the exact timing, a Nd:YAG laser was synchronized with the high-speed camera by a delay generator. Spray-guided injectors were applied in the optically accessible engine.

2.2. Particle image velocimetry (PIV) system

The configuration of the PIV system is shown in Fig. 3. A laser sheet with a thickness of 2 mm was formed by a planar concave lens (PCV) and a planar convex lens (PCX). The laser sheet passed through the middle of the cylinder between the intake valves, as shown in Fig. 3(b). There was a region covered by liner housing, even though the engine cylinder was made of transparent quartz. Therefore, the width of the PIV image plane (65 mm) was slightly smaller than that of the bore (75.6 mm). The captured PIV raw images were processed using a code written in MATLAB (PIVlab, MathWorks, USA) [16]. Additional functions to calculate tumble center, tumble ratio, and turbulent kinetic energy were added to the existent code. One of the important parts of processing PIV raw images is cross-correlation algorithm. The cross correlation that is a statistical pattern matching technique is used to find the particle pattern in an image pair. In this study, this pattern matching technique was conducted by using the discrete cross correlation function as follows [17]:

Table 2
Specifications of the PIV system.

Items	Details
Camera	High-speed camera (Phantom, VEO 710L)
Laser	Nd:YAG pulse laser (26 mJ, double cavity)
Region of interest	65×100 mm
Resolution	320×344 pixels
Seed	$10 \ \mu m$, hollow sphere glass
PIV image time interval (δt)	Intake stroke: $20 \ \mu s$
	Compression stroke: $40 \ \mu s$
Interrogation area	32×32 pixels (50% overlap)
Correlation algorithm	FFT (Fast Fourier Transform)

$$C(m, n) = \sum_i \sum_j A(i, j) B(i - m, j - n) \qquad \text{Eq.1}$$

where A and B are interrogation areas from image A (first image) and image B (second image). This discrete cross-correlation function can be solved in the spatial or frequency domain [17,18]. In this study, the particle displacement was detected using fast Fourier transform cross-correlation coupled with a 2×3-point algorithm to reduce the computational cost. The number of vectors of the flow field in the combustion chamber was derived from minimum 280 to maximum 1330. However, only a quarter of total vectors was drawn for the visibility of flow field except for Fig. 5. The details of the specifications of the PIV system are listed in Table 2 [19].

2.3. Vector field computation

Even though the in-cylinder flow of a real engine is three-dimensional, the PIV image plane, which is a vertical plane, is useful for comprehending tumble flow. This is because the main motion of the tumble flow is two-dimensional. Therefore, the tumble center, tumble ratio, and effective radius were calculated at the vertical PIV plane for quantitative analysis of in-cylinder flow.

2.3.1. Tumble center (TC)

The tumble center (TC) is defined as the position with maximum moment summation (MS), given by Eq. (2) [19]. The mean TC was used to represent the TC of the mean in-cylinder flow.

$$MS = \sum_{i=1}^n \sum_{j=1}^m \left(\left(\vec{r}_{i,j} - \vec{r}_{r,c} \right) \times \vec{V}_{i,j} \right) \qquad \text{Eq.2}$$

where (r, c) is a position in the vector field.

2.3.2. Tumble ratio (TR)

The tumble ratio (TR) was calculated based on the TC. The equation used to calculate TR is as follows [19]:

$$TR = \frac{\sum_{i=1}^n \sum_{j=1}^m \left(\vec{r}_{i,j} - \vec{r}_{tc} \right) \times \vec{V}_{i,j}}{\omega \sum_{i=1}^n \sum_{j=1}^m \left(\vec{r}_{i,j} - \vec{r}_{tc} \right) \cdot \left(\vec{r}_{i,j} - \vec{r}_{tc} \right)} \qquad \text{Eq.3}$$

where $(\vec{r}_{i,j} - \vec{r}_{tc})$ is the distance of a given location with indices (i, j) from the center of rotation, $(\vec{r}_{i,j} - \vec{r}_{tc})$ is the distance of a given
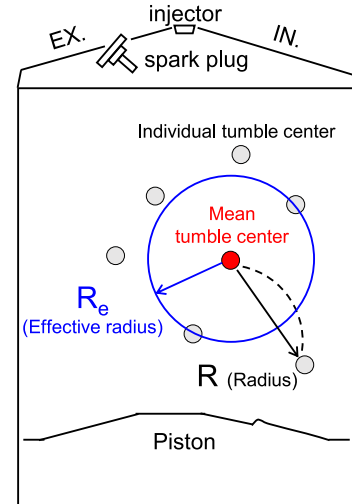

Fig. 4. Definition of effective radius.

location with indices (i, j) from the image center, $\vec{V}_{i,j}$ is the velocity at a given location with indices (i, j), and ω is the angular velocity of the engine. By calculating the TR, we can determine the intensity of the in-cylinder flow rotation.

2.3.3. Effective radius (R_e)

In this study, an effective radius (R_e) was defined to quantitatively analyze the variation in TC. The effective radius is the average of the distance from the mean TC to the individual TC. Therefore, the larger the variation in TC, the larger the effective radius is. Fig. 4 presents a description of the effective radius. The effective radius is calculated as follows:

$$R_e = \left(\sum_1^n R \right) \bigg/ n \qquad \text{Eq.4}$$

where R is the distance from the mean TC to the individual TC and n is the number of cycles used for averaging.

2.4. Experimental conditions

In this study, the engine speed, intake pressure, and IVO timing were varied to analyze the in-cylinder flow depending on the engine operating conditions. The optically accessible engine has a fixed cam duration. In the case of the reference IVO timing condition, the intake valves open from bTDC $332°–114°$ without overlap between the intake and exhaust valves. In the case of the advanced IVO timing condition, the intake valves opened 40 crank angle degrees (CAD) earlier than in the reference condition. The exhaust valve timing was fixed from aTDC $152°–370°$. The PIV measurements were performed for the entire range of intake strokes to compression strokes before spark timing. The details of the experimental conditions are listed in Table 3.
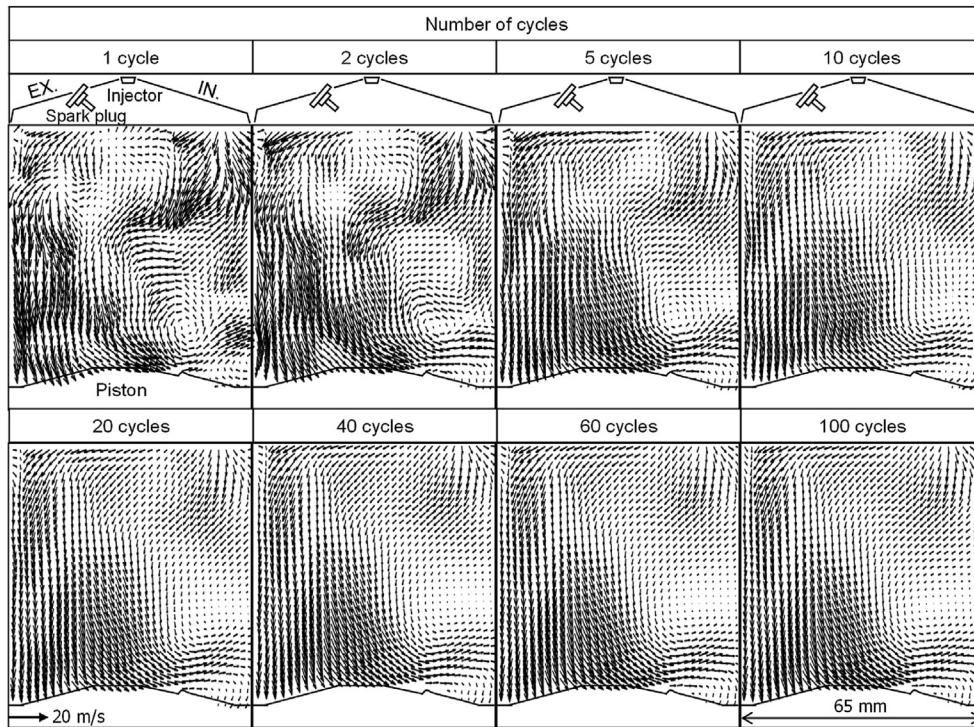
Fig. 5. Mean in-cylinder flow as a function of the number of individual cycles (@ w/o injection, 1 500 rpm, P_{intake}: 1.0 bar, IVO timing: reference, bTDC 210°).

Table 3
Experimental conditions.

Items	Details	
Engine speed (rpm)	1500, 1800, 2000	
Intake pressure (bar)	0.8, 1.0, 1.3	
Intake valve timing (bTDC, °)	Reference IVO	IVO: 332, IVC: 114
	Advanced IVO	IVO: 372, IVC: 154
	Retarded IVO	IVO: 292, IVC: 74
Exhaust valve timing (aTDC, °)	EVO: 152, EVC: 370	
Intake air temperature (°C)	35	
Injection pressure (bar)	700	
Fuel temperature (°C)	90	

3. Results and discussion

In this study, the CCV under different engine operating conditions was investigated by calculating the mean velocity, TR, TC, and effective radius. The engine speed, manifold pressure, and intake valve timing were selected as engine operating parameters because these parameters define the basic operating conditions for a GDI engine.

3.1. Characteristics of mean in-cylinder flow and CCV

The mean in-cylinder flow as a function of the number of individual cycles used for averaging is depicted in Fig. 5. As the number of individual cycles used for averaging increased, the mean in-cylinder flow field stabilized, and the structure of the mean in-cylinder flow field converged after approximately 20 cycles. The
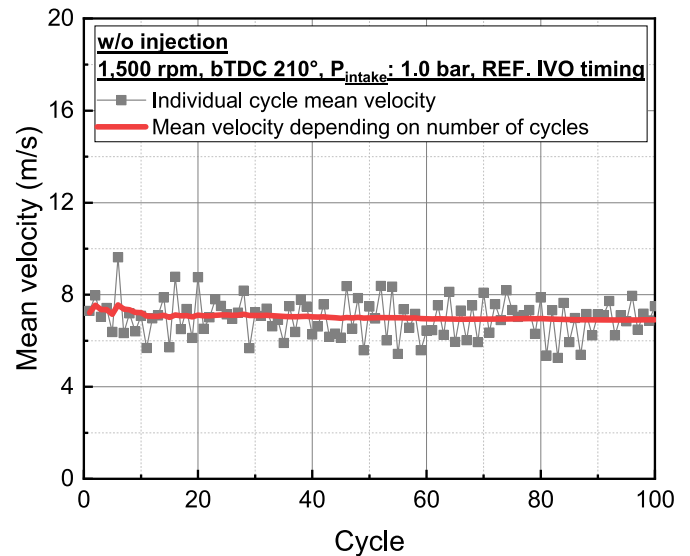

Fig. 6. Mean velocity as a function of the number of individual cycles used for averaging (@ w/o injection, 1 500 rpm, P_{intake}: 1.0 bar, IVO timing: reference, bTDC = 210°).

mean velocity, which depends on the number of individual cycles used for averaging, is shown in Fig. 6. Similar to the mean in-cylinder flow, the mean velocity converged after approximately 20 cycles. Therefore, in this study, considering the accuracy and efficiency of the experiment, a mean in-cylinder flow of 60 cycles
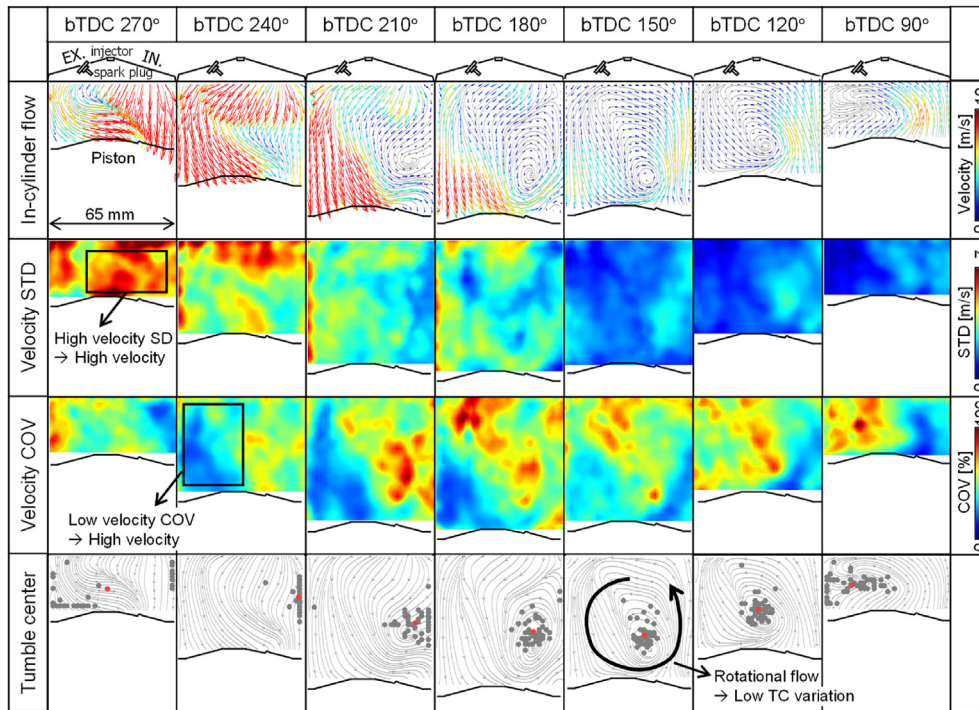
Fig. 7. Mean velocity, velocity SD, velocity COV, and TC depending on the crank angle (@ w/o injection, 1500 rpm, P intake: 1.0 bar, IVO timing: reference).
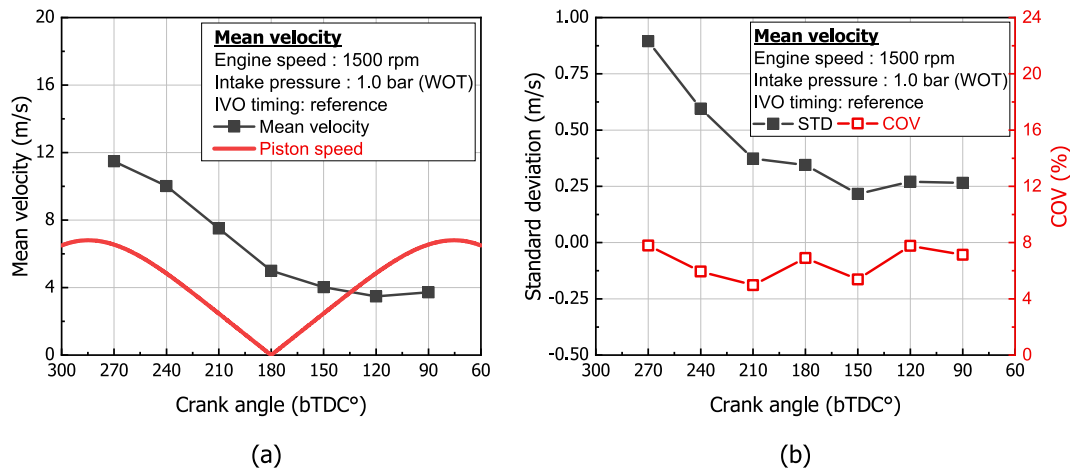

Fig. 8. Mean velocity, SD, and COV of mean velocity: (a) mean velocity, and (b) SD and COV (@ w/o injection, 1500 rpm, P_{intake}: 1.0 bar, IVO timing: reference).

was selected as a representative in-cylinder flow.

The mean in-cylinder flow, velocity standard deviation (SD) distribution, velocity coefficient of variance (COV) distribution, and TC are depicted in Fig. 7. In the early stage of the intake strokes (before bTDC 210°), the intake air flowed into the cylinder with high momentum through the top surface of the intake valves. The intake valves were opened less to narrow their outlet area. Therefore, a high velocity developed at the upper side of the cylinder. The rotational flow was generated in the middle stage of the intake

stroke, while the intake valves were opened gradually. The flow velocity at the upper side of the cylinder decreased because the outlet area of the intake valves was wider, and the suction force caused by the descending piston decreased. A high SD was observed in the early stage of intake strokes, especially in the high-velocity region. However, the velocity COV was low at the main flow, which had a relatively high velocity. The mean TC at bTDC 270° was located on the left or right side. This is because the main flow with a high velocity alternated from the left side to the right
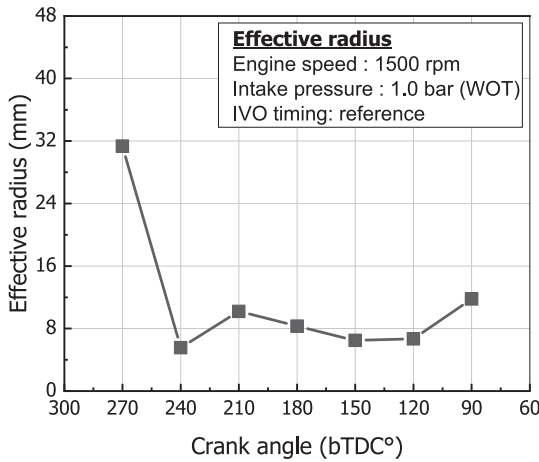
Fig. 9. Effective radius depending on the crank angle (@ w/o injection, 1 500 rpm, P_{intake}: 1.0 bar, IVO timing: reference).

side, and the rotational flow had not formed. As the rotational flow formed, the TC moved to the center of the cylinder, and the variation in TC decreased.

In Fig. 8(a), the mean velocity decreased continuously during the intake strokes owing to the dissipation of momentum supplied during the early stage of intake strokes. This is because there was no additional momentum supply. The mean velocity decreased below the piston speed after bTDC 150°. However, during the compression stroke, the piston moved upward, so that the mean in-cylinder flow was slightly increased at bTDC 90°, which is near the maximum piston speed. The SD of the mean velocity was high at the early stage of the intake stroke because the in-cylinder flow had a relatively high velocity, as shown in Fig. 8(b). However, a similar level of COV was observed during intake and compression strokes. These results indicate that the level of in-cylinder flow variation

was similar during the intake and compression strokes.

The effective radius with respect to the crank angle is shown in Fig. 9. The effective radius decreased after bTDC 270° because tumble flow occurred. When the main flow achieved a sufficiently high velocity, tumble flow, which is a rotational flow, occurred, and the in-cylinder flow was stable and repeatable. The TR, which depends on the crank angle, is depicted in Fig. 10(a). The TR increased after bTDC 270° owing to the descending piston. As the distance between the piston top and intake valves increased, the rotational flow could be formed easily because of the decrease in the collision between the intake air and the piston top. Similar to the effective radius results, the SD and COV of TR also decreased after bTDC 270°, showing similar levels, as shown in Fig. 10(b).

3.2. Effects of engine speed on CCV

The optically accessible engine was operated below 2000 rpm because of the risk of damage. Fig. 11(a) shows the mean in-cylinder flow depending on the engine speed. The structure of the in-cylinder flow remained the same at all engine speeds. The COV distribution was also insignificantly affected by the engine speed and showed a similar distribution irrespective of the engine speed.

An ideal mixture formation can be formed by the interaction between the in-cylinder flow and the spray. The injected fuel has a relatively high density compared to the air, so a main flow with high velocity plays an important role as a fuel carrier because it has a relatively high momentum. Therefore, understanding the main flow with high velocity is important for devising an injection strategy and making an ideal mixture formation. Under all engine speed conditions, a low COV was observed in the high-velocity region regardless of the crank angle, as shown in Fig. 11(b). The mean in-cylinder flow velocities increased slightly as the engine speed increased, as shown in Fig. 12(a). During the intake strokes, the slope of the velocity drop at 2000 rpm was steeper than that at 1500 rpm because of the rapid momentum loss. In contrast, the mean velocity at 2000 rpm was more accelerated than that at
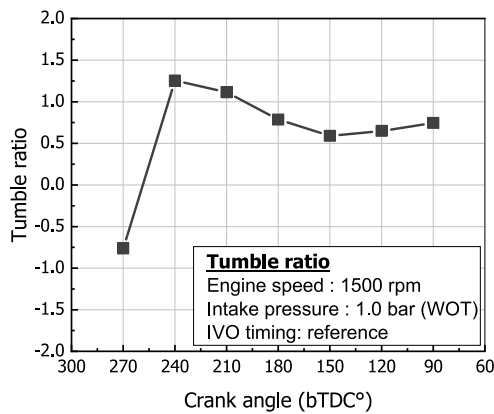
(a)
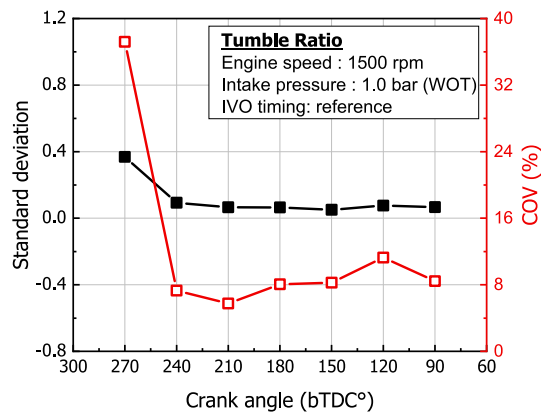
(b)

Fig. 10. TR, SD, and COV depending on the crank angle: (a) TR and (b) SD and COV of TR (@ w/o injection, 1500 rpm, P_{intake}: 1.0 bar, IVO timing: reference).
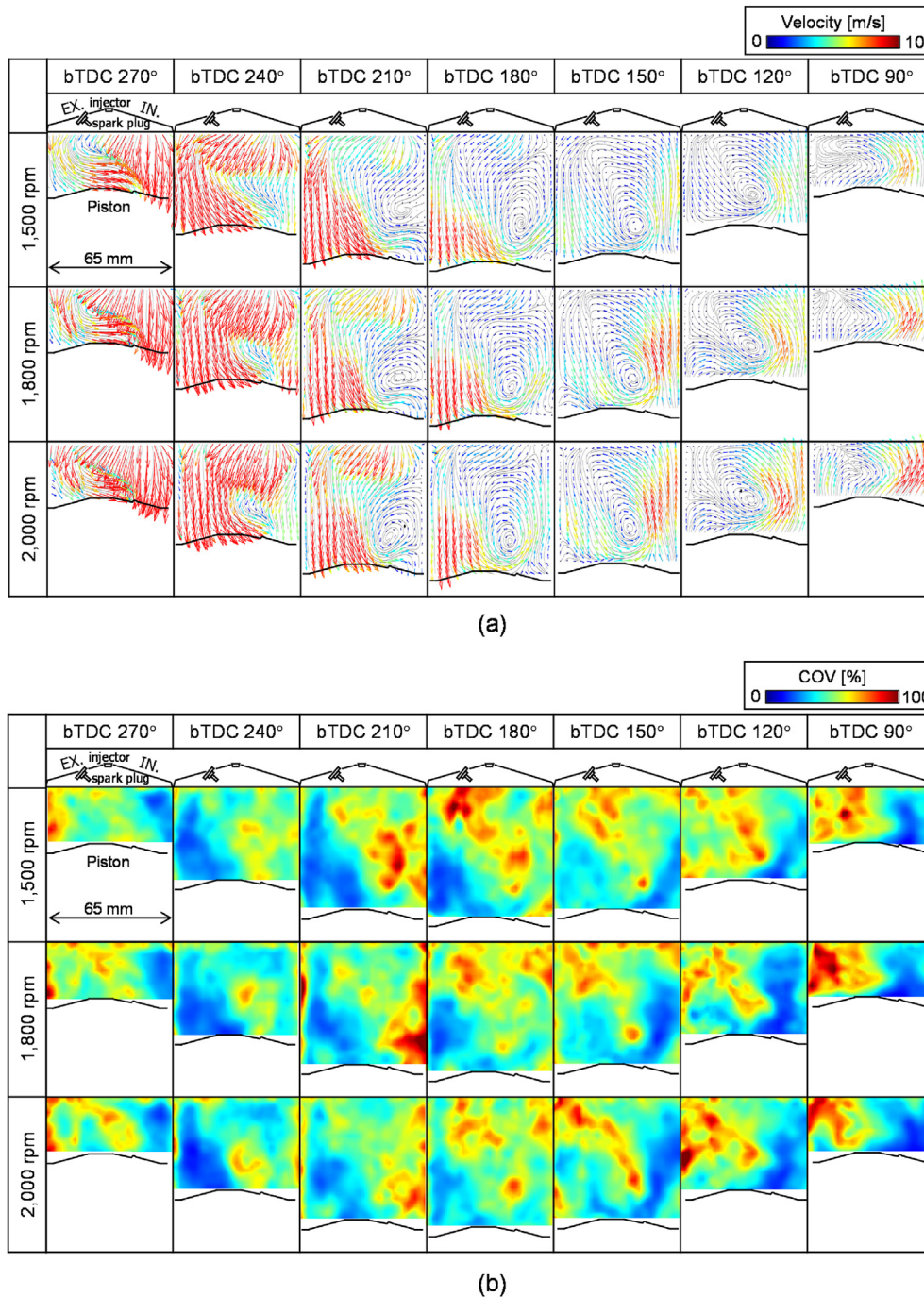
Fig. 11. Mean in-cylinder flow and velocity COV distribution depending on the engine speed: (a) mean in-cylinder flow and (b) velocity COV distribution (@ w/o injection, P$_{intake}$: 1.0 bar, IVO timing: reference).

1500 rpm during the compression strokes because of the fast piston movement, which supplies additional energy to the in-cylinder flow. The SD also slightly increased as the engine speed increased, as shown in Fig. 12(b). The SD was relatively high during the early stages of intake strokes.

Fig. 13 shows the variation in the TC at each crank angle depending on the engine speed. The TC travel path depending on the crank angle was similar regardless of the engine speed because the engine speed could not significantly affect the structure of the in-cylinder flow. At both engine speeds, the variation in the TC was high at bTDC 270° because the rotational flow was not completely formed. The variation in TC decreased when the in-cylinder flow rotated. The variation in TC at 2000 rpm was similar to that at 1500 rpm, except for the bTDC 90°. The in-cylinder flow at
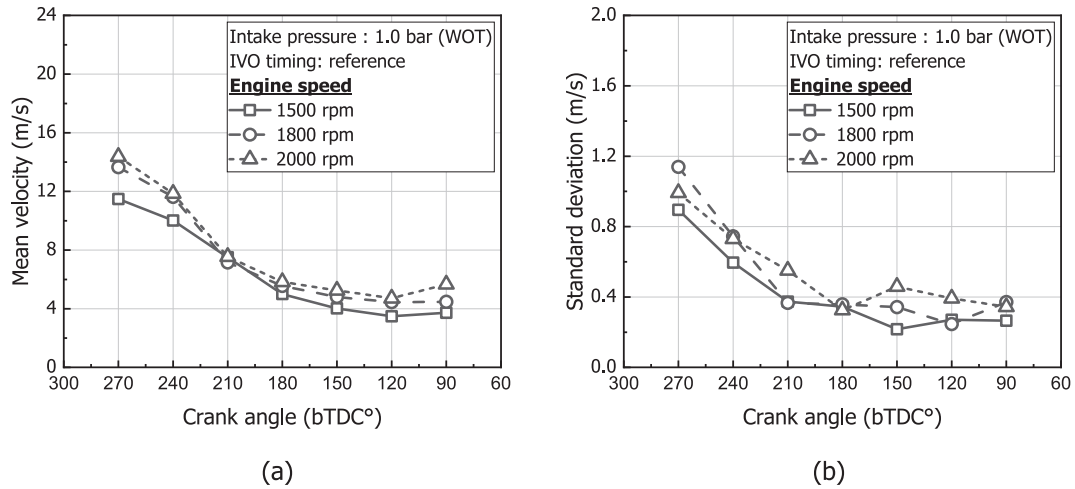
Fig. 12. Mean velocity and SD depending on the engine speed: (a) mean velocity and (b) SD of mean velocity (@ w/o injection, P_{intake}: 1.0 bar, IVO timing: reference).
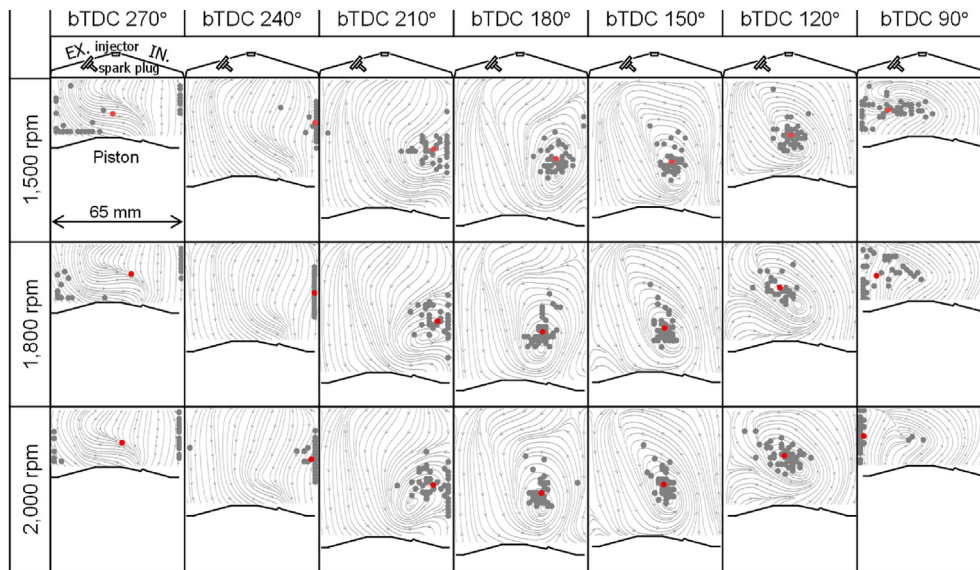

Fig. 13. TC and variation of TC depending on the engine speed(@ w/o injection, P_{intake}: 1.0 bar, IVO timing: reference).

2000 rpm was stronger on the right side than that at 1500 rpm because of the fast piston movement, so that the TC was concentrated on the left side.

The variation in TC was analyzed quantitatively by calculating the effective radius, as shown in Fig. 14. The effective radius was the highest at bTDC 270°, which was before the formation of rotational flow. After the rotational flow was formed, the effective radius rapidly decreased. The effective radius had a similar level regardless of the engine speed. From these results, we can infer that the TC variation was not significantly affected by the in-cylinder flow intensity under the similar structure of the in-cylinder flow condition.

The results of the TC are useful for understanding the results of the TR in Fig. 15(a) because the TR was calculated based on the TC.

The magnitude of TR at 2000 rpm was slightly lower than that at 1500 rpm. This means that the angular velocity of in-cylinder flow did not increase as much as the angular velocity of the engine did when engine speed increased. There was no difference in the SD of TR depending on the crank angle, as shown in Fig. 15(b). The SD of TR was low after the tumble flow was formed, after bTDC 270°. From the results of TC and TR, we can see that the tumble flow decreased the in-cylinder flow variation and resulted in repetitive and stable in-cylinder flow.

3.3. Effects of intake pressure on in-cylinder flow

The engine load can be controlled by the intake pressure (air mass) and the amount of fuel. The injected fuel moves with the in-
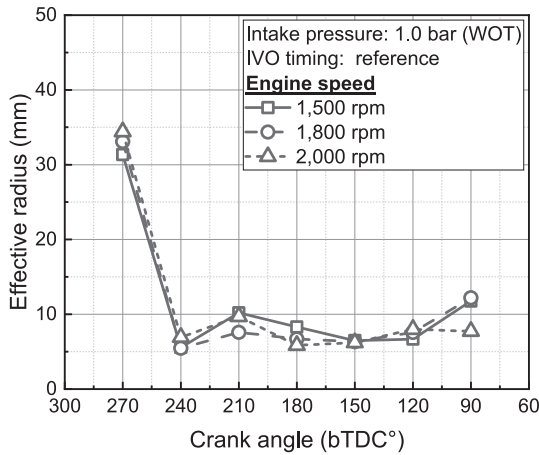
Fig. 14. Effective radius depending on the engine speed (@ w/o injection, P_{intake}: 1.0 bar, IVO timing: reference).

cylinder flow; thus, the comprehension of the in-cylinder flow characteristics is important. In this research, the visualization of the in-cylinder flow was conducted from an intake pressure of 0.8−1.3 bar. The mean in-cylinder flow and velocity COV distributions depending on the intake pressure are shown in Fig. 16. The in-cylinder flow structure did not change even though the intake pressure changed, as shown in Fig. 16(a).

The injection strategy was optimized by considering the factors affecting the mixture formation. An important factor is the interaction between the in-cylinder flow and spray [20]. Therefore, to comprehend this interaction, the in-cylinder flow should be analyzed preferentially. In this context, the in-cylinder flow structure not changing with a change in intake pressure change is a significant result. We can reasonably predict the results when the optimized injection strategy from naturally aspirated (NA) conditions is applied to boosting conditions. As the intake pressure

increased, the velocity COV distribution also showed a similar form without significant difference, as shown in Fig. 16(b). This is because one of the main factors affecting the velocity COV distribution is the structure of the in-cylinder flow, which remained unchanged.

The mean velocities at intake pressures of 1.0 and 1.3 bar were increased slightly compared with those at an intake pressure of 0.8 bar during the intake strokes, as shown in Fig. 17(a). However, the results under NA conditions are close to those obtained under boosting conditions. There was no significant difference in the SD of the mean velocity depending on the intake pressure, as shown in Fig. 17(b).

Fig. 18 shows the TC and TC variation depending on the intake pressure. At all intake pressures, the TC moved from the right side to the left side during the intake and compression strokes. Moreover, as the rotational flow was formed, the variation in TC decreased. As the intake pressure increased, the in-cylinder flow was slightly intensified owing to the fast outlet velocity at the intake valves caused by the pressure difference between the in-cylinder and manifold. Therefore, the rotational flow was intensified, resulting in a decrease in TC variation during the compression stroke.

The results of the effective radius, which is a quantitative index indicating the variation in TC, are depicted in Fig. 19. The effective radius slightly decreased during the compression stroke as the intake pressure increased owing to the intensified in-cylinder flow, especially when the in-cylinder flow rotated. However, the in-cylinder flow continuously loses momentum from the intake stroke to the compression stroke. Therefore, the effective radius was shown to be similar at bTDC 90°, even though the in-cylinder flow was slightly intensified.

The TR and SD of TR depending on the intake pressure are shown in Fig. 20. The TR increased as the intake pressure increased owing to the intensified rotational flow, as shown in Fig. 20(a). However, the TR converged to a similar level at bTDC 90° owing to the continuous momentum loss. The SD of the TR was similar,
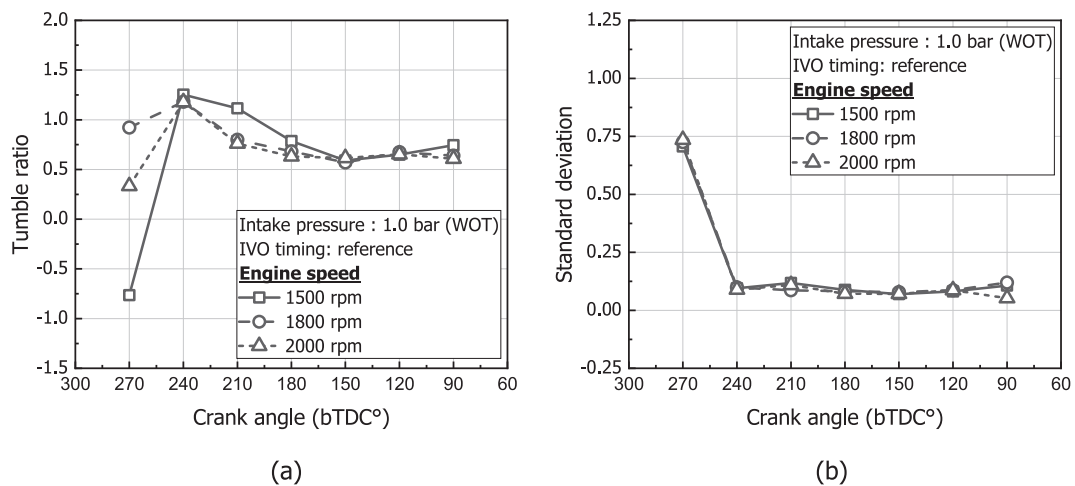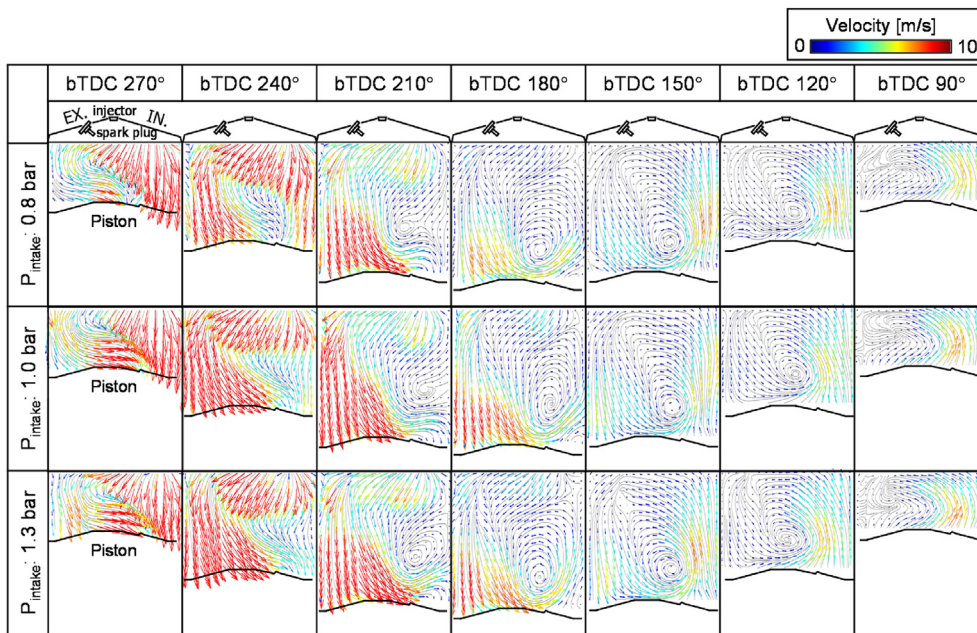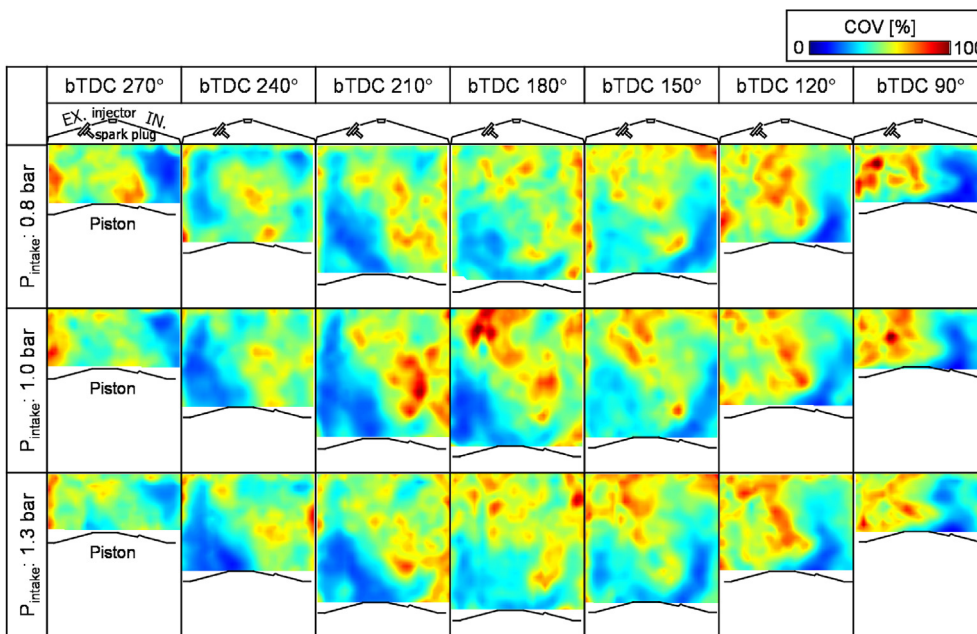

(a)

(b)

Fig. 15. TR and SD depending on the crank angle: (a) TR and (b) SD of TR (@ w/o injection, P_{intake}: 1.0 bar, IVO timing: reference).

Fig. 16. Mean in-cylinder flow and velocity COV distribution depending on the intake pressure: (a) mean in-cylinder flow and (b) velocity COV distribution (@ w/o injection, 1 500 rpm, IVO timing: reference).

except for bTDC 270°. In the case of an intake pressure of 1.3 bar, the TC was located on the right side with a relatively high probability during 60 cycles, so that the SD of TR was lower than that of the other cases.

3.4. Effects of IVO timing on CCV

In recent GDI engines, valve timing plays an important role in increasing combustion efficiency [21,22]; therefore, various techniques, such as variable valve timing (VVT) [23,24] and
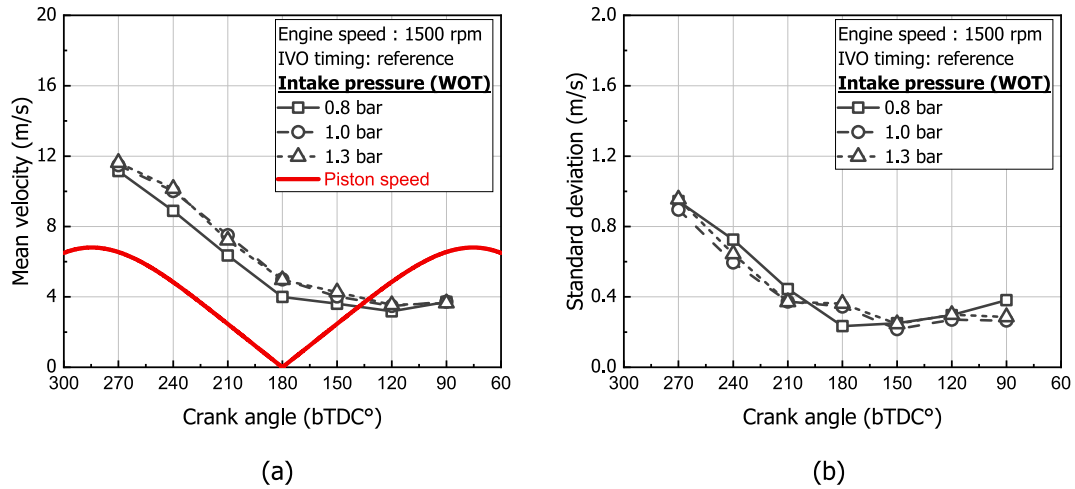
Fig. 17. The mean velocity and SD depending on the intake pressure: (a) mean velocity and (b) SD of mean velocity (@ w/o injection, 1500 rpm, IVO timing: reference).
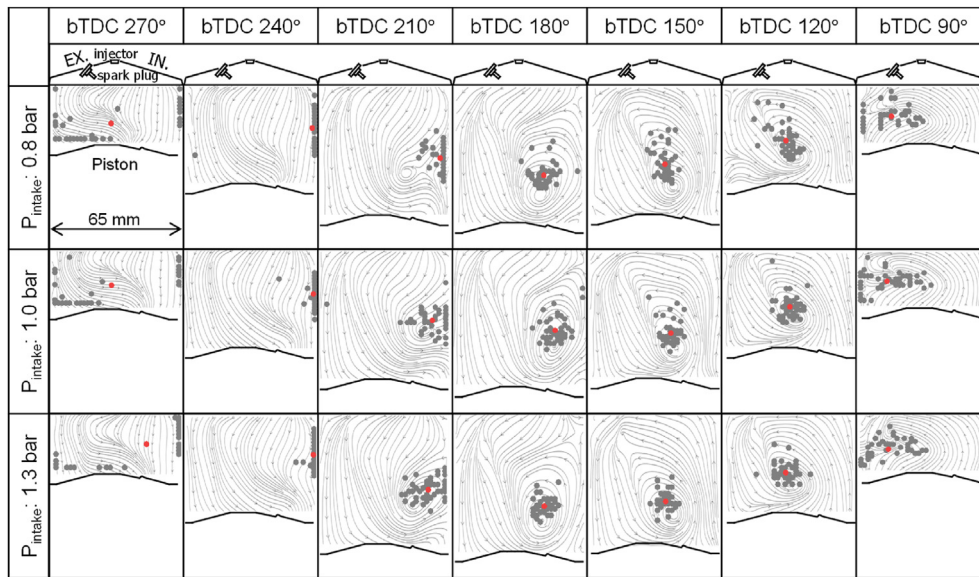

Fig. 18. TC and variation of TC depending on the intake pressure(@ w/o injection, 1500 rpm, IVO timing: reference).

continuously variable valve lift (CVVL) [25], and until recently, Hyundai Motor Company's unique Continuous Variable Valve Duration (CVVD) [26,27] system have been developed. In this study, the intake valve timing, which is the most significant parameter for optimizing the engine volumetric efficiency, was selected as one of the engine operating parameters to confirm the tendency of in-cylinder flow. The test engine had a fixed cam duration.

Fig. 21 shows the mean in-cylinder flow and velocity COV distributions as a function of the IVO timing. In the case of the advanced IVO condition, the valve lift is larger than in other conditions in the region where the piston speed is fast, as shown in Fig. 22. Therefore, owing to the wide inlet area, the initial inflow air velocity was relatively low. During the compression strokes, the intake valves were completely closed after bTDC 154°. The in-

cylinder flow of the advanced IVO timing is close to the in-cylinder flow of the reference IVO timing, even though there is no backflow during the compression strokes. In the case of the advanced IVO timing, the velocity COV distribution was also observed to have a similar distribution to the reference IVO timing, as shown in Fig. 21(b). This is because the structure of the in-cylinder flow in the case of advanced IVO timing was similar to that of the reference IVO timing.

In the case of the retarded IVO timing, in the early stage of the intake strokes around the maximum piston speed, the intake valve is opened below 2 mm, which is much lower than other IVO timing conditions (Fig. 22). Therefore, the mean in-cylinder flow velocity was more than double that of the reference IVO or advanced IVO conditions, as shown in Fig. 23(a). As the intake flow was fast, it
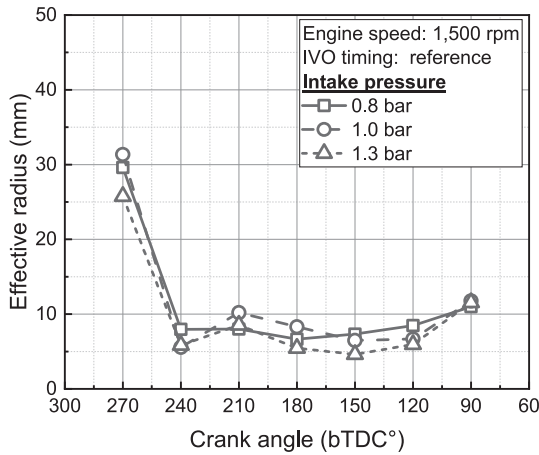
Fig. 19. Effective radius depending on the intake pressure (@ w/o injection, 1 500 rpm, IVO timing: reference).

collided with the piston head, such that the in-cylinder flow that winds from outside to inside was formed following the piston head at bTDC 270°. With the descending piston, the collision between the intake flow and piston head decreased, resulting in the strong intake air flowing straight into the cylinder following the liner. The in-cylinder velocity dramatically decreased after the early stage of the intake stroke. This is because the intake air mass was relatively low; thus, the supplied momentum could not be maintained over a long period. The velocity COV distribution was different compared to the advanced and reference IVO timing conditions because of the difference in the structure of the in-cylinder flow. During the transition from the intake stroke to the compression stroke, a weak rotational flow with a relatively low velocity was formed. Therefore, the velocity COV was relatively high in the entire region of the cylinder compared to the other IVO timing conditions. Even though the structure of the in-cylinder flow and velocity COV distribution

were different under the retarded IVO conditions, the tendency to show low COV in the high-velocity region was the same as that under other IVO timing conditions (Fig. 21(b)).

The mean velocity and SD depending on the IVO timing are depicted in Fig. 23. As the IVO timing was retarded, the mean velocity increased during the early stage of the intake stroke. However, owing to the continuous momentum loss, the mean in-cylinder velocity showed a similar level during the compression stroke (Fig. 23(a)). Owing to the high in-cylinder flow velocity, the SD was highest at the early stage of the intake stroke under the retarded IVO timing condition, as shown in Fig. 23(b). However, the SD of the mean velocity rapidly decreased after bTDC 240° owing to the decrease in mean velocity.

The variation in TC is related to the intensity of the rotational flow. When the in-cylinder flow rotates strongly, the variation in the TC decreases. During the compression stroke, the variation in TC under the retarded IVO condition was higher than that under other IVO timing conditions, as shown in Fig. 24. This is because the rotational flow was not sufficiently developed under the retarded IVO condition during the progression from the intake stroke to the compression stroke. In the case of advanced IVO timing, the rotational flow developed early because the intake valves were opened early. Therefore, a low variation in TC at bTDC 210° and bTDC 180° was observed. The results shown in Fig. 24 were quantitatively confirmed by calculating the effective radius, as shown in Fig. 25. The effective radius after bTDC 210°, which is the period of forming the rotational flow, was distinctly different depending on the IVO timing. In the retarded IVO timing condition, which did not form the rotational flow, the variation in TC was more than double that of other IVO timing conditions. However, the difference in effective radius between the IVO timing conditions decreased during the compression stroke. This is because in all IVO timing conditions, the rotational flow was weakened owing to the momentum loss.

The TR was calculated based on the TC; thus, the TR was highest at bTDC 240° under the retarded IVO conditions, as shown in Fig. 26(a). The TR rapidly decreased after bTDC 240°, and showed a
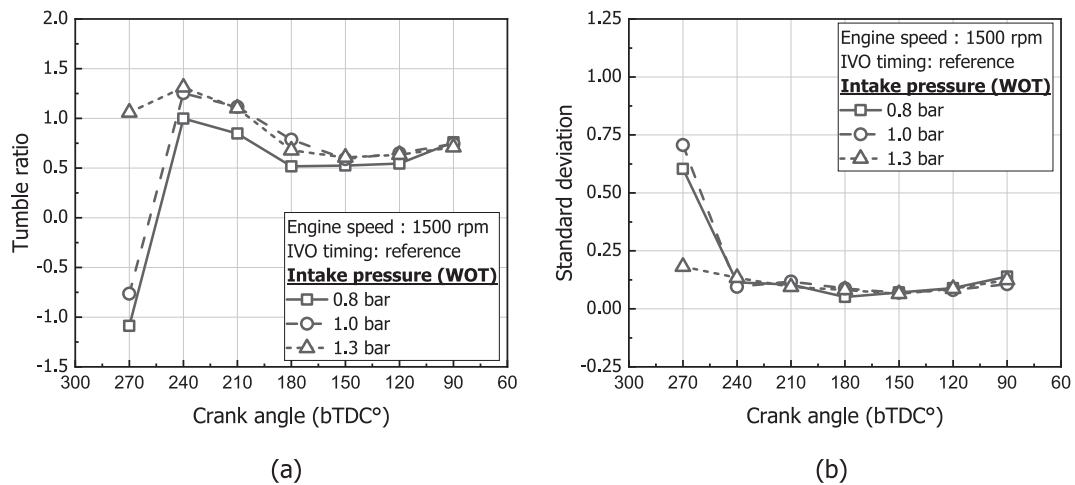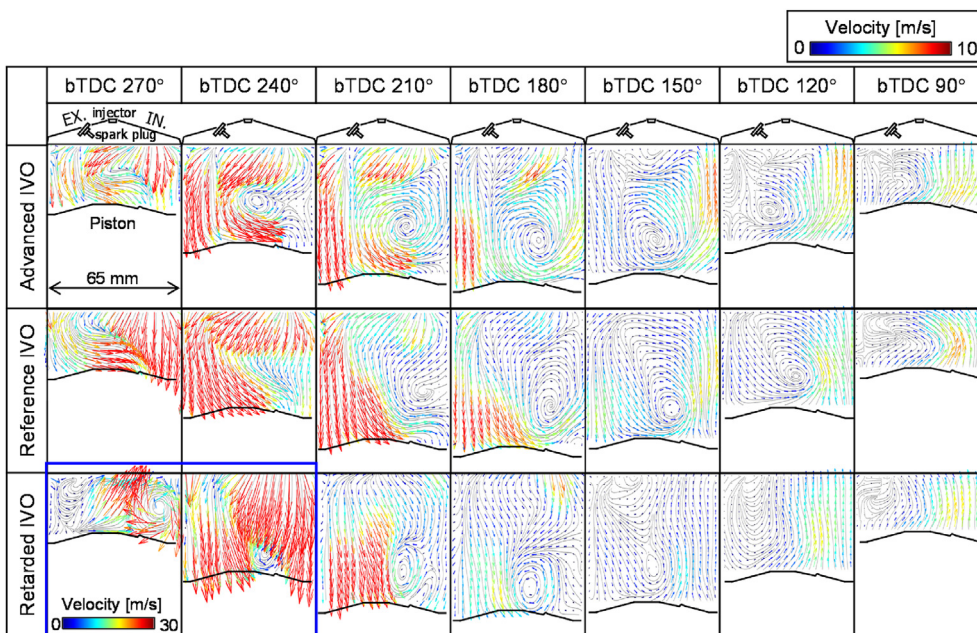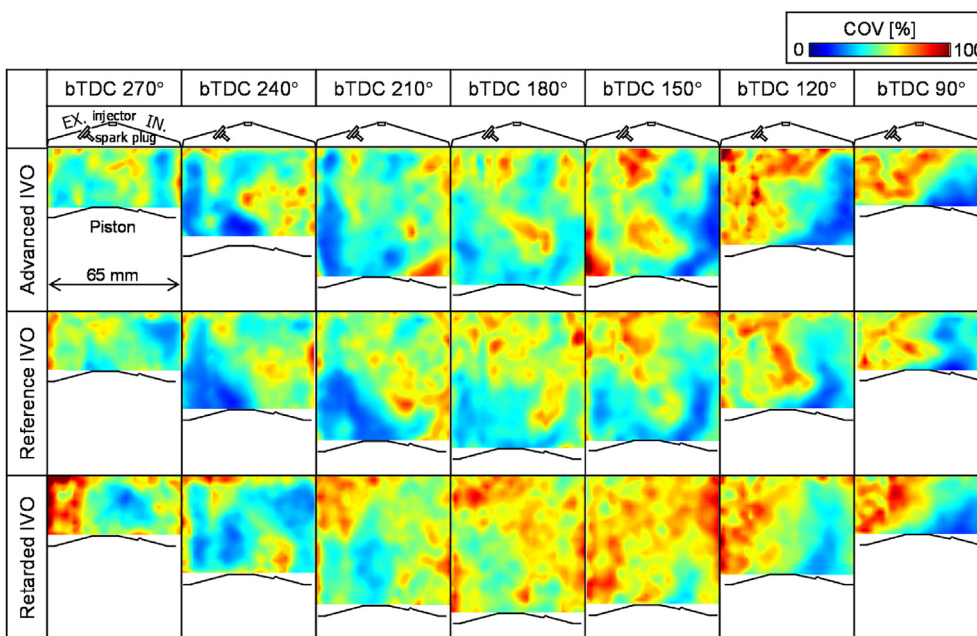

(a)

(b)

Fig. 20. TR and SD depending on the intake pressure: (a) TR and (b) SD of TR (@ w/o injection, 1 500 rpm, IVO timing: reference).

Fig. 21. Mean in-cylinder flow and velocity COV distribution depending on the IVO timing: (a) mean in-cylinder flow and (b) velocity COV distribution (@ w/o injection, 1 500 rpm, P_{intake}: 1.0 bar).

level similar to other IVO timing conditions at bTDC 90°. The SD of TR was slightly higher than that of other IVO timing conditions during the compression stroke owing to the relatively high variation in TC.

3.5. Effects of fuel injection on CCV

Fuel injection significantly affects the in-cylinder flow because a high momentum is additionally supplied into the cylinder. The
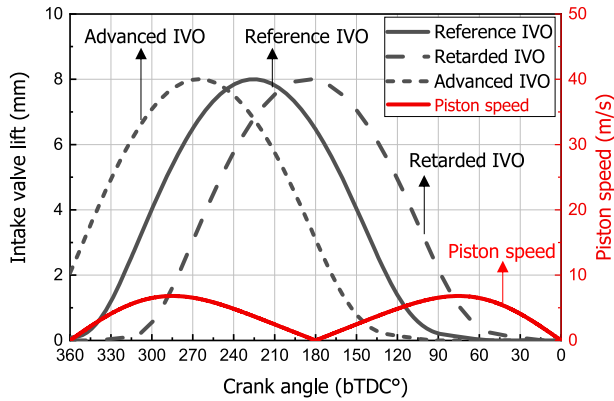
Fig. 22. Intake valve lift profiles and piston speed at 1500 rpm.

intensity and structure of the in-cylinder flow can be changed by fuel injection. However, the effects of fuel injection on in-cylinder flow, such as injection timing and targeting, can differ according to the injection strategy [28,29]. Therefore, in this study, the effects of fuel injection on the CCV were analyzed under different injection conditions.

The in-cylinder flow, velocity COV distribution, and TC after fuel injection are shown in Fig. 27. The in-cylinder flow was intensified and strongly rotated by the fuel injection. The low COV region occurred in the high-velocity region, similar to the result of the in-cylinder flow without fuel injection. The TC was located in the middle of the cylinder, and the variation in TC was relatively low or similar to that without fuel injection conditions owing to the strong rotational flow. The effective radius was compared with and without fuel injection conditions, as shown in Fig. 28. Immediately
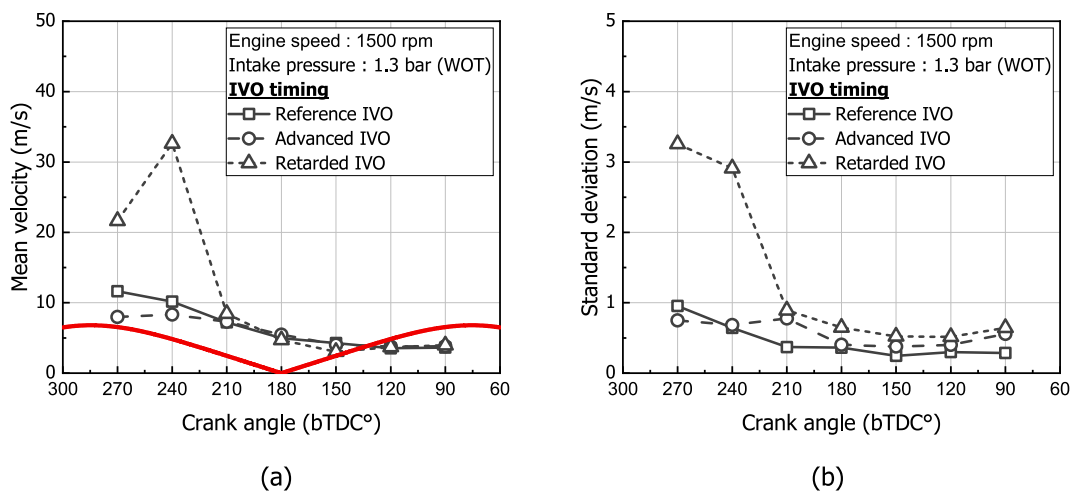

(a)

(b)

Fig. 23. Mean velocity and SD depending on the IVO timing: (a) mean velocity and (b) SD of mean velocity (@ w/o injection, 1500 rpm, P_{intake}: 1.0 bar).
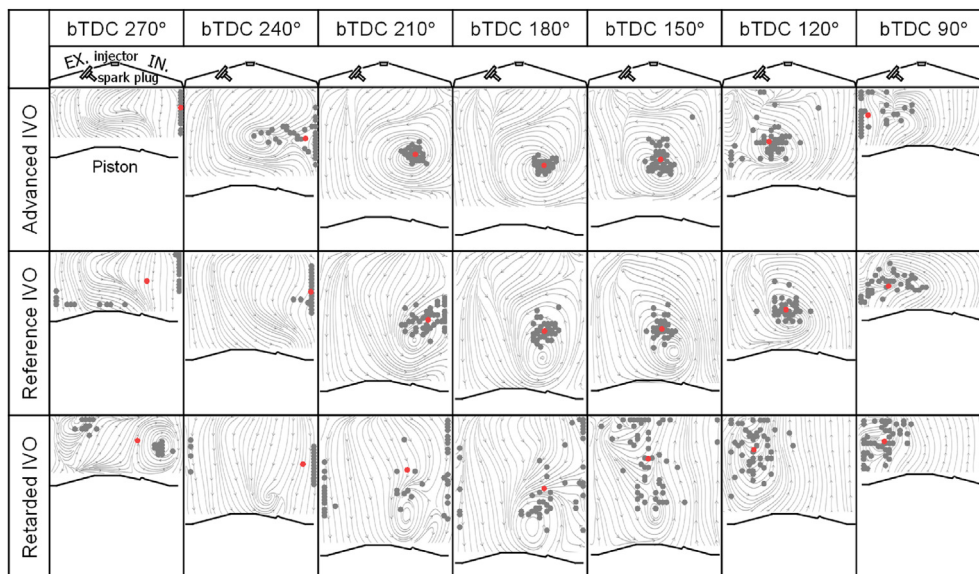

Fig. 24. TC and variation of TC depending on the IVO timing (@ w/o injection, 1500 rpm, P_{intake}: 1.0 bar).
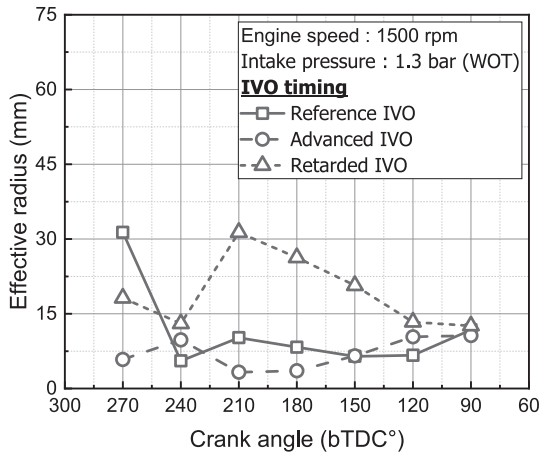
Fig. 25. Effective radius depending on the IVO timing (@ w/o injection, 1500 rpm, P_intake: 1.0 bar).

formed. As a result, the effective radius after 30 CAD of fuel injection was similar to or higher than that without fuel injection conditions, as shown in Fig. 30. Conversely, in the case of the side-mounted injector, a strong rotational flow can be formed immediately after fuel injection because the fuel is injected in only one direction [30]. Therefore, a stable and repeatable in-cylinder flow can be formed.

In this study, the in-cylinder flow at bTDC 90°, depending on the injection timing, was analyzed, as shown in Fig. 31. The rotational flow was intensified when the fuel was injected earlier than bTDC 120°. However, as the injection timing was close to bTDC 90°, an ascending flow occurred. A low COV region was observed in the high-velocity region, similar to the results of the in-cylinder flow without fuel injection.

Fig. 32 shows the effective radius at bTDC 90° depending on the injection timing. The effective radius under the fuel injection condition was lower than that without fuel injection in all injection timing conditions. At bTDC 300°, which is an early injection for the

(a)

(b)

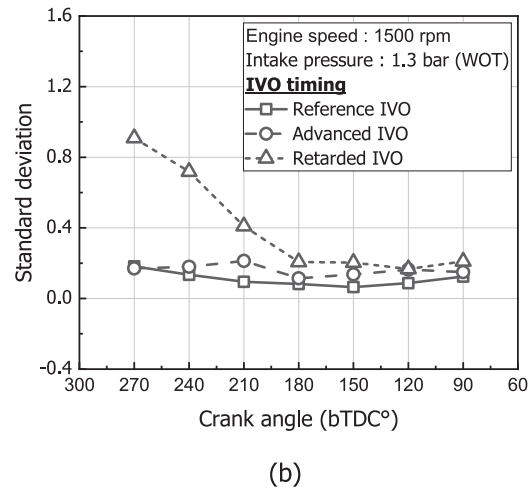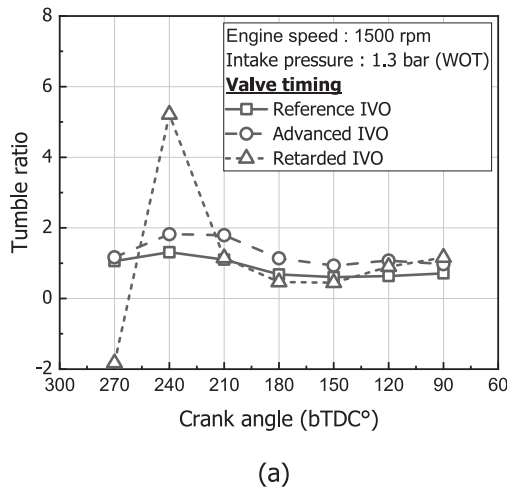Fig. 26. TR and SD depending on the IVO timing: (a) TR and (b) SD of TR (@ w/o injection, 1500 rpm, P_intake: 1.0 bar).

after the fuel injection, at bTDC 240°, the effective radius did not decrease. However, the in-cylinder flow with high momentum was formed by the fuel injection; thus, the rotational flow was maintained throughout the compression stroke. As a result, the effective radius was low even when continuous momentum loss occurred during the compression stroke.

Fig. 29 shows the in-cylinder flow, velocity COV distribution, and TC after 30 CAD of fuel injection. Immediately after fuel injection, the in-cylinder flow was intensified, and a low COV region was formed in the high-velocity region. However, the variation in TC did not decrease because rotational flow did not form immediately. The test injector was a spray-guided injector, which is a center-mounted injector. Therefore, rather than the rotational flow, the flow that rises from the outside of the cylinder to the center was

fuel injection condition, the effective radius was similar both with fuel injection and without fuel injection. This is because continuous momentum loss occurred over a relatively long time, from bTDC 300°−90°. When the fuel was injected at bTDC 150°, a strong rotational flow was formed at bTDC 90°, resulting in the lowest effective radius. However, if the injection timing was retarded further until bTDC 120°, ascending flow rather than rotational flow occurred at bTDC 90°. Therefore, the effective radius increased compared to that of bTDC 150°.

The in-cylinder flow, velocity COV distribution, and TC at bTDC 90° under various engine operating conditions with fuel injection are shown in Fig. 33. In all cases, the in-cylinder flow was intensified by fuel injection at bTDC 270°, and a low COV region was observed in the high-velocity region. The effective radius at bTDC
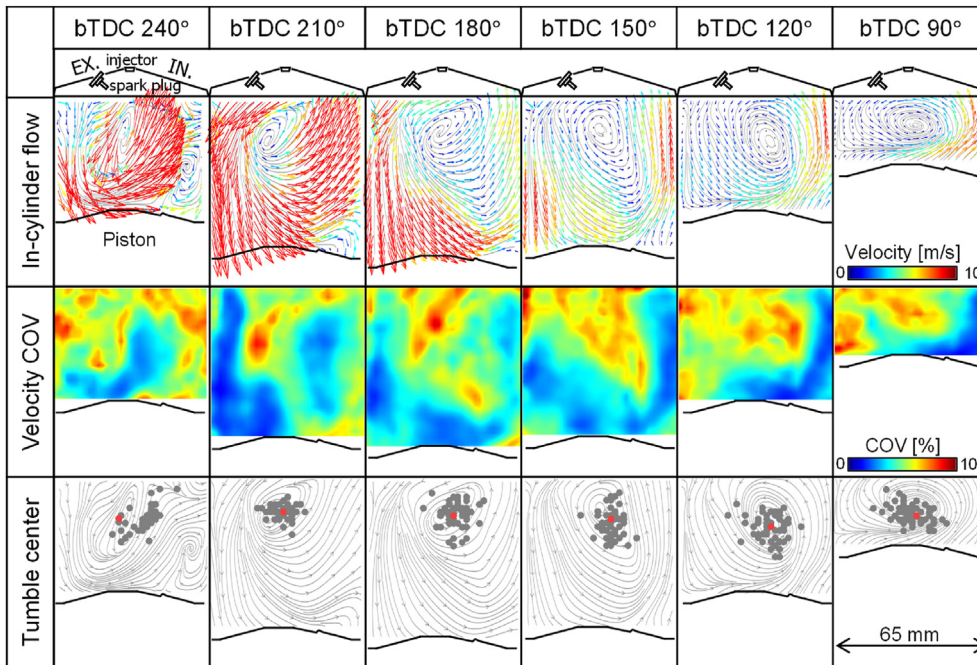
Fig. 27. In-cylinder flow, velocity COV distribution and TC after fuel injection (@ w/injection, SOE: bTDC 270°, 1500 rpm, P_{inj}: 700 bar, P_{intake}: 1.0 bar, IVO timing: reference, lambda: 1).
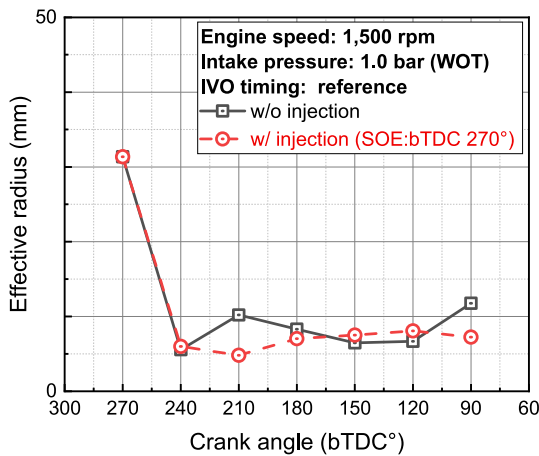

Fig. 28. Effective radius depending on the crank angle after fuel injection (@ w/injection, SOE: bTDC 270°, 1500 rpm, P_{inj}: 700 bar, P_{intake}: 1.0 bar, IVO timing: reference, lambda: 1).

90° with fuel injection was lower than that at bTDC 90° without fuel injection in all cases, as shown in Fig. 34. Therefore, we confirmed that fuel injection could decrease the CCV even when the spray-guided injection was applied.
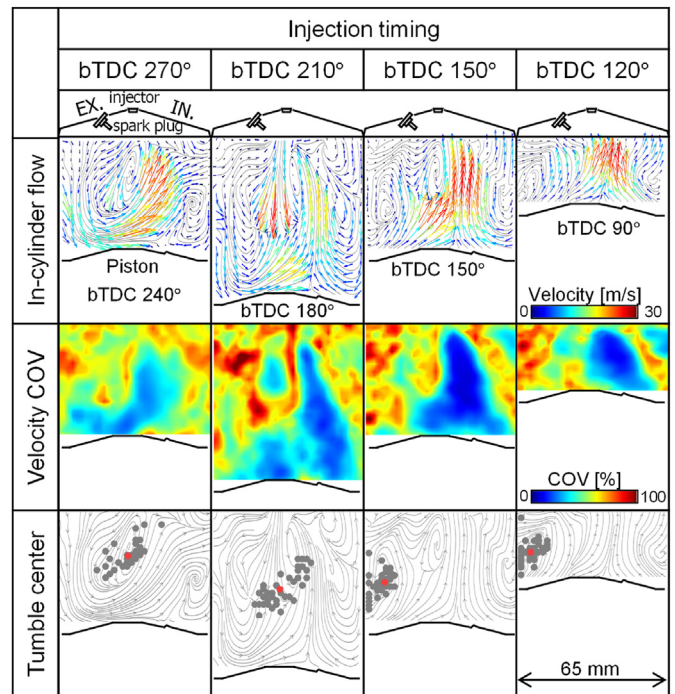

Fig. 29. In-cylinder flow, velocity COV distribution and TC after 30 CAD of fuel injection (@ w/injection, SOE: bTDC 270°, 1500 rpm, P_{inj}: 700 bar, P_{intake}: 1.0 bar, IVO timing: reference, lambda: 1).
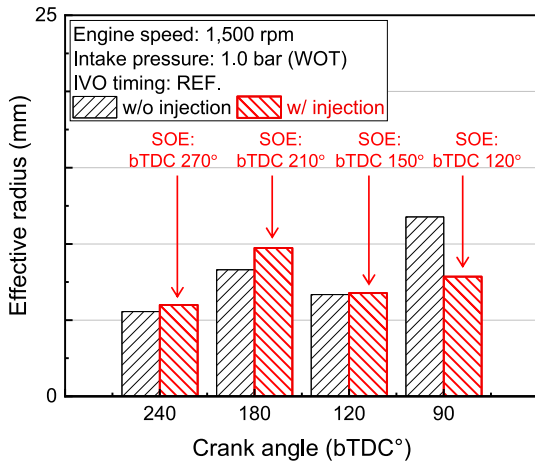
Fig. 30. Effective radius after 30 CAD of fuel injection under different injection timing conditions (@ w/injection, SOE: bTDC 270°, 1500 rpm, P_{inj}: 700 bar, P_{intake}: 1.0 bar, IVO timing: reference, lambda: 1).
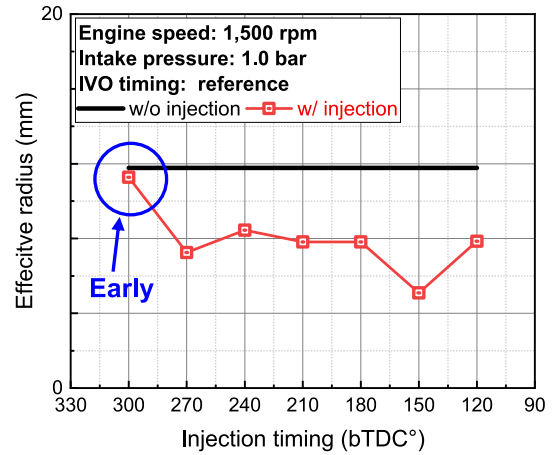

Fig. 32. Effective radius at bTDC 90° after fuel injection with various injection timings (@ w/injection, SOE: bTDC 270°, 1500 rpm, P_{inj}: 700 bar, P_{intake}: 1.0 bar, IVO timing: reference, lambda: 1).
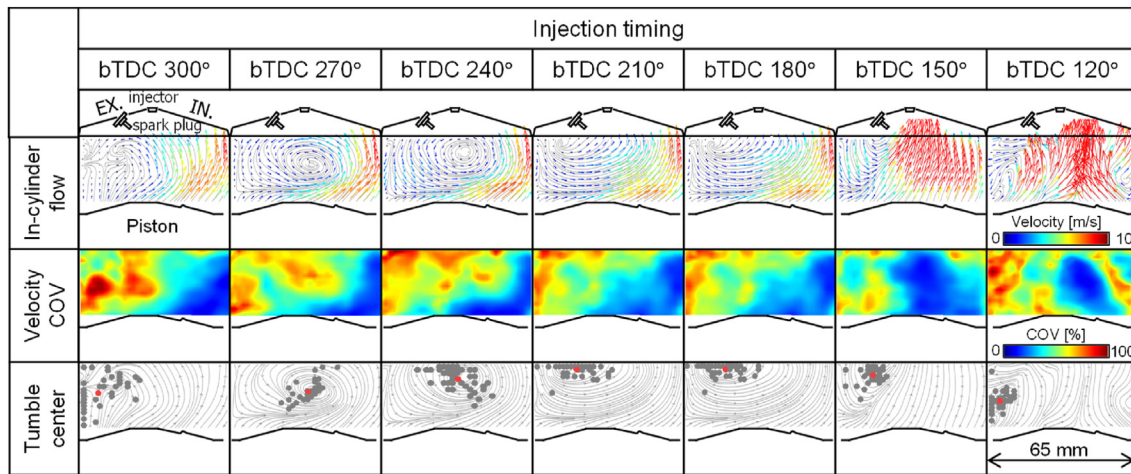

Fig. 31. In-cylinder flow, velocity COV distribution, and TC at bTDC 90° after fuel injection with various injection timing (@ w/injection, SOE: bTDC 270°, 1500 rpm, P_{inj}: 700 bar, P_{intake}: 1.0 bar, IVO timing: reference, lambda: 1).

4. Conclusions

In this study, the CCV of the in-cylinder flow in a spark-assist high-compression-ratio spray-guided DI engine was investigated based on the engine operating conditions of engine speed, intake pressure, and intake valves timing using PIV measurements. Moreover, the effects of fuel injection on the CCV were analyzed quantitatively by calculating the in-cylinder flow mean velocity, TR, TC, and effective radius. The following conclusions were drawn:

- The effective radius was affected by structure of in-cylinder flow and intensity of rotational flow. The effective radius was low level when the in-cylinder flow rotated strongly. The low-velocity COV region of the in-cylinder flow velocity was observed in the high-velocity region regardless of the engine operating conditions.

- An increase in the engine speed caused an increase in the in-cylinder flow velocity owing to the fast piston movement. The structure of the in-cylinder flow and the effective radius remained similar even when the engine speed increased.

- An increase in the intake pressure led to a slight increase in the in-cylinder flow velocity. However, there was no clear difference in the in-cylinder flow structure and effective radius.

- The structure and velocity of in-cylinder flow were significantly affected by the IVO timing conditions. The timing occurring high velocity was changed, so that the structure of in-cylinder flow was varied. Especially, in the case of the retarded IVO conditions, a weak rotational flow developed during the compression
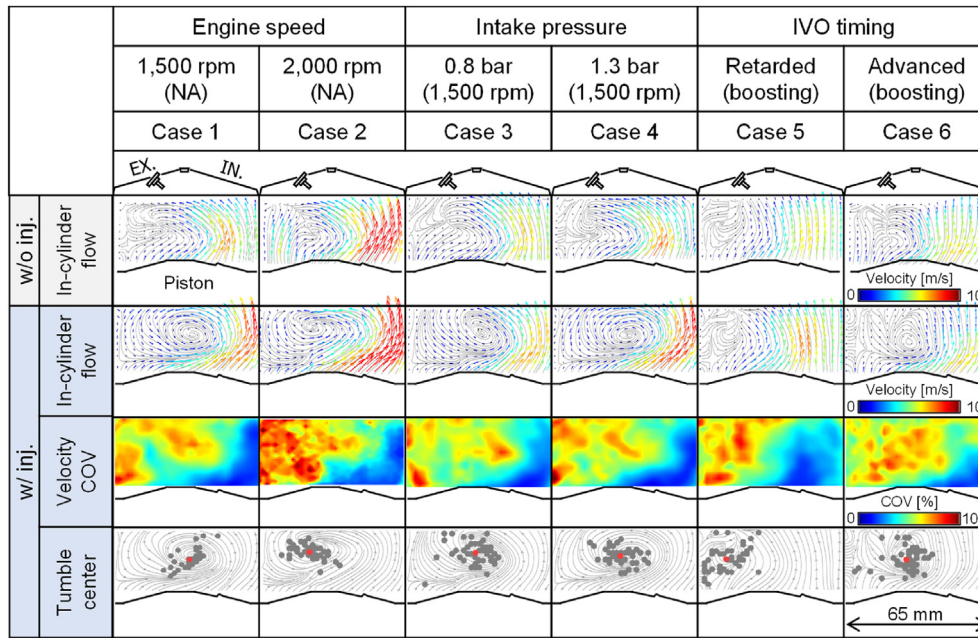
		Engine speed		Intake pressure		IVO timing	
		1,500 rpm (NA)	2,000 rpm (NA)	0.8 bar (1,500 rpm)	1.3 bar (1,500 rpm)	Retarded (boosting)	Advanced (boosting)
		Case 1	Case 2	Case 3	Case 4	Case 5	Case 6

Fig. 33. In-cylinder flow, velocity COV distribution, and TC at bTDC 90° after fuel injection with various injection timings (@ w/injection, SOE: bTDC 270°, 1500 rpm, P_{inj}: 700 bar, P_{intake}: 1.0 bar, IVO timing: reference, lambda: 1).
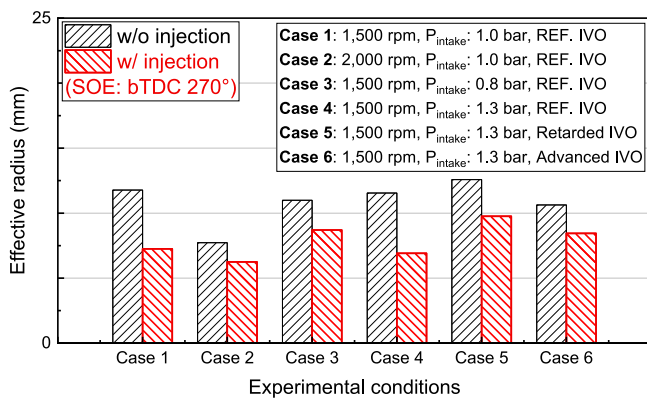

Fig. 34. Effective radius at bTDC 90° after fuel injection (@ w/injection, SOE: bTDC 270°, 1500 rpm, P_{inj}: 700 bar, P_{intake}: 1.0 bar, IVO timing: reference, lambda: 1).

stroke, such that a high effective radius was observed as compared to reference and advanced IVO conditions.
- The fuel injection affected the in-cylinder flow intensity and structure. The in-cylinder flow was intensified after fuel injection. However, the effective radius did not decrease immediately, because the rotational flow did not develop immediately after fuel injection. However, the effective radius at bTDC 90° after fuel injection at bTDC 270° was lower than the effective radius without fuel injection regardless of the engine operating conditions.

Author contribution

Donghwan Kim: Writing – original draft preparation, Investigation, Experiments, Yousang Son: Conceptualization, Methodology, Sungwook Park: Writing- Reviewing and Editing, Supervision.

Declaration of competing interest

The authors declare that they have no known competing financial interests or personal relationships that could have appeared to influence the work reported in this paper.

Acknowledgement

References

[1] Awad OI, et al. Particulate emissions from gasoline direct injection engines: a review of how current emission regulations are being met by automobile manufacturers. Sci Total Environ 2020;718:137302. https://doi.org/10.1016/j.scitotenv.2020.137302.

[2] Duan X, et al. A review of controlling strategies of the ignition timing and combustion phase in homogeneous charge compression ignition (HCCI) engine. Fuel 2021;285. https://doi.org/10.1016/j.fuel.2020.119142.

[3] Peterson B, et al. Assessment and application of tomographic PIV for the spray-induced flow in an IC engine. Proc Combust Inst 2017;36(3):3467–75. https://doi.org/10.1016/j.proci.2016.06.114.

[4] Park C, et al. Stratified lean combustion characteristics of a spray-guided

combustion system in a gasoline direct injection engine. Energy 2012;41(1): 401−7. https://doi.org/10.1016/j.energy.2012.02.060.

[5] Fansler TD, et al. Invited Review: combustion instability in spray-guided stratified-charge engines: a review. Int J Engine Res 2015;16(3):260−305. https://doi.org/10.1177/1468087414565675.

[6] He X, et al. Impact of coolant temperature on piston wall-wetting and smoke generation in a stratified-charge DISI engine operated on E30 fuel. Proc Combust Inst 2019;37(4):4955−63. https://doi.org/10.1016/j.proci.2018.07.073.

[7] Geschwindner C, et al. Analysis of the interaction of Spray G and in-cylinder flow in two optical engines for late gasoline direct injection. Int J Engine Res 2019;21(1):169−84. https://doi.org/10.1177/1468087419881535.

[8] Kazmouz SJ, et al. Large-eddy simulations of a stratified-charge direct-injection spark-ignition engine: comparison with experiment and analysis of cycle-to-cycle variations. Proc Combust Inst 2021;38(4):5849−57. https://doi.org/10.1016/j.proci.2020.08.035.

[9] Bendu H, Murugan S. Homogeneous charge compression ignition (HCCI) combustion: mixture preparation and control strategies in diesel engines. Renew Sustain Energy Rev 2014;38:732−46. https://doi.org/10.1016/j.rser.2014.07.019.

[10] Liu H, et al. Effects of temperature inhomogeneities on the HCCI combustion in an optical engine. Appl Therm Eng 2011;31(14−15):2549−55. https://doi.org/10.1016/j.applthermaleng.2011.04.020.

[11] Hasan MM, Rahman MM. Homogeneous charge compression ignition combustion: advantages over compression ignition combustion, challenges and solutions. Renew Sustain Energy Rev 2016;57:282−91. https://doi.org/10.1016/j.rser.2015.12.157.

[12] Parthasarathy M, et al. Performance analysis of HCCI engine powered by tamanu methyl ester with various inlet air temperature and exhaust gas recirculation ratios. Fuel 2020;282:118833. https://doi.org/10.1016/j.fuel.2020.118833.

[13] Aydoğan B. An experimental examination of the effects of n-hexane and n-heptane fuel blends on combustion, performance and emissions characteristics in a HCCI engine. Energy 2020;192:116600. https://doi.org/10.1016/j.energy.2019.116600.

[14] https://insidemazda.mazdausa.com/press-release/mazda-next-generation-technology-press-information/.

[15] Heywood JB. Internal combustion engine fundamentals. McGraw-Hill Education; 2018.

[16] Thielicke W, Stamhuis EJ. PIVlab − towards user-friendly, affordable and accurate digital particle image velocimetry in MATLAB. J Open Res Software 2014;2. https://doi.org/10.5334/jors.bl.

[17] Huang H, Dabiri D, Gharib M. On errors of digital particle image velocimetry. Meas Sci Technol 1997;8(12):1427. https://doi.org/10.1088/0957-0233/8/12/007.

[18] Soria J. An investigation of the near wake of a circular cylinder using a video-based digital cross-correlation particle image velocimetry technique. Exp Therm Fluid Sci 1996;12(2):221−33. https://doi.org/10.1016/0894-1777(95)00086-0.

[19] Kim D, et al. Characteristics of in-cylinder flow and mixture formation in a high-pressure spray-guided gasoline direct-injection optically accessible engine using PIV measurements and CFD. Energy Convers Manag 2021;248:114819. https://doi.org/10.1016/j.enconman.2021.114819.

[20] Clark LG, et al. The effect of fuel-injection timing on in-cylinder flow and combustion performance in a spark-ignition direct-injection (SIDI) engine using particle image velocimetry (PIV). Flow, Turbul Combust 2018;101(1):191−218. https://doi.org/10.1007/s10494-017-9887-x.

[21] Osorio JD, Rivera-Alvarez A. Efficiency enhancement of spark-ignition engines using a Continuous Variable Valve Timing system for load control. Energy 2018;161:649−62. https://doi.org/10.1016/j.energy.2018.07.009.

[22] Tripathy S, Das A, Srivastava DK. Electro-pneumatic variable valve actuation

system for camless engine: Part II-fuel consumption improvement through un-throttled operation. Energy 2020;193:116741. https://doi.org/10.1016/j.energy.2019.116741.

[23] Hong H, Parvate-Patil G, Gordon B. Review and analysis of variable valve timing strategies—eight ways to approach. Proc Inst Mech Eng - Part D J Automob Eng 2004;218(10):1179−200. https://doi.org/10.1177/095440700421801013.

[24] Yuan Z, et al. Quantitative study on influence factors of power performance of variable valve timing (VVT) engines and correction of its governing equation. Energy 2018;157:314−26. https://doi.org/10.1016/j.energy.2018.05.135.

[25] Li Q, et al. Comparative study on the pumping losses between continuous variable valve lift (CVVL) engine and variable valve timing (VVT) engine. Appl Therm Eng 2018;137:710−20. https://doi.org/10.1016/j.applthermaleng.2018.04.017.

[26] Rajput O, et al. Numerical analysis of a six-stroke gasoline compression ignition (GCI) engine combustion with continuously variable valve duration (CVVD) control. In: Internal combustion engine division fall technical conference. American Society of Mechanical Engineers; 2018. https://doi.org/10.1115/ICEF2018-9590.

[27] Shin W, et al. An experimental study on a six-stroke gasoline homogeneous charge compression ignition (HCCI) engine with continuously variable valve duration (CVVD). 2021. https://doi.org/10.4271/2021-01-0512. SAE Technical Paper.

[28] Keskinen K, et al. Mixture formation in a direct injection gas engine: numerical study on nozzle type, injection pressure and injection timing effects. Energy 2016;94:542−56. https://doi.org/10.1016/j.energy.2015.09.121.

[29] Oh H, Bae C. Effects of the injection timing on spray and combustion characteristics in a spray-guided DISI engine under lean-stratified operation. Fuel 2013;107:225−35. https://doi.org/10.1016/j.fuel.2013.01.019.

[30] Sevik J, et al. Influence of injector location on part-load performance characteristics of natural gas direct-injection in a spark ignition engine. SAE Int J Engines 2016;9(4):2262−71. https://doi.org/10.4271/2016-01-2364.

Nomenclature

P_{intake}: Intake pressure

Abbreviations

aTDC: After Top Dead Center
bTDC: Before Top Dead Center
CCV: Cycle-to-cycle Variation
CI: Compression Ignition
COV: Coefficient of Variable
CVVL: Continuously Variable Valve Lift
DI: Direct Injection
EVC: Exhaust Valve Closing
EVO: Exhaust Valve Opening
GDI: Gasoline Direct Injection
HCCI: Homogeneous Charge Compression Ignition
IVC: Intake Valve Closing
IVO: Intake Valve Opening
PCL: Planar Convex Lens
PCV: Planar Concave Lens
SD: Standard Deviation
SPCCI: Spark Controlled Compression Ignition
TKE: Turbulent Kinetic Energy
TR: Tumble Ratio
VVT: Variable Valve Timing